The Astrophysical Journal Supplement Series, 264:24 (14pp), 2023 January https://doi.org/10.3847/1538-4365/aca325

WISE Green Objects (WGOs): The Massive Star Candidates in the Whole Galactic Plane ($|b| < 2°$)

Chang Zhang[1,2], Guo-Yin Zhang[1], Jin-Zeng Li[1], and Jing-Hua Yuan[1]
[1] National Astronomical Observatories, Chinese Academy of Sciences, A20 Datun Road, Chaoyang District, Beijing 100101, People's Republic of China
zhangc@nao.cas.cn, zgyin@nao.cas.cn, ljz@naocas.cn
[2] University of Chinese Academy of Sciences, Beijing 100049, People's Republic of China
Received 2022 June 28; revised 2022 November 8; accepted 2022 November 11; published 2023 January 11

Abstract

Massive young stellar objects (MYSOs) play a crucial role in star formation. Given that MYSOs were previously identified based on the extended structure and the observational data for them is limited, screening the Wide-field Infrared Survey Explorer (WISE) objects showing green features (for the common coding of the 4.6 μm band as the green channel in three-color composite WISE images) will yield more MYSO candidates. Using WISE images in the whole Galactic plane ($0° < l < 360°$ and $|b| < 2°$), we identified sources with strong emissions at the 4.6 μm band, then according to morphological features divided them into three groups. We present a catalog of 2135 WISE Green Objects (WGOs). 264 WGOs have an extended structure. 1366 WGOs show compact green features but without extended structure. 505 WGOs have neither extended structure nor green features, but the intensity at 4.6 μm is numerically at least 4.5 times that of 3.4 μm. According to the analysis of the coordinates of WGOs, we find WGOs are mainly distributed in $|l| < 60°$, coincident with the position of the giant molecular clouds in $|l| > 60°$. Matching results with various masers show that those three groups of WGOs are at different evolutionary stages. After crossmatching WGOs with published YSO survey catalogs, we infer that ∼50% of WGOs are samples of newly discovered YSOs. In addition, 1260 WGOs are associated with Hi-GAL sources, according to physical parameters estimated by spectral energy distribution fitting, of which 231 are classified as robust MYSOs and 172 as candidate MYSOs.

Unified Astronomy Thesaurus concepts: Star formation (1569); Massive stars (732); Infrared sources (793); Protostars (1302)

Supporting material: machine-readable tables

1. Introduction

As the main contributor to emission and the chemical enrichment of the universe, the formation of stars has invariably been an important research topic in astronomy. The scenario of low-mass star formation has been well established (Shu et al. 1987). Statistics suggest that massive star formation is unlikely to be found nearby, with most being >2 kpc away. As the influence of factors such as star-forming regions are rare and deeply embedded, the timescales are extremely short, and the natal environments are inevitably destroyed by violent feedback, the formation processes of massive stars ($\gtrsim 8\,M_\odot$) is still a mystery (Zinnecker & Yorke 2007). The result of these observational obstacles is that there are few accurate or well-selected samples of objects in the early stages of evolution. A large, unbiased sample of massive young stellar objects (MYSOs), especially those in infancy, could help understand the processes involved in the formation and earliest stages of massive star formation (Urquhart et al. 2014, 2022).

The "monolithic collapse" model (McKee & Tan 2002, 2003) and the "competitive accretion" model (Bonnell et al. 1997; Bonnell & Greaves 2004) are two popular models of massive star formation. The monolithic collapse model is an extended version of low-mass star formation, in which gas is accreted onto the protostar through an accretion disk at a significantly higher rate of accretion compared to its low-mass star formation. The final stellar mass comes from the initial core mass in this model. The competitive accretion model is that massive stars always form in clusters and rely on the competitive accumulation of cluster members from a common envelope. The final stellar mass depends on the result of the competition. Regardless of the mass, there is evidence of the same nature of low- and high-mass star formation. For example, the latest findings of accretion bursts in MYSO (e.g., Caratti o Garatti et al. 2017; Stecklum et al. 2017, 2021) reveal that both low- and high-mass protostars form through disk accretion, accompanied by episodic accretion bursts, possibly caused by disk fragmentation. The typical accretion rate during the low-mass star formation is $\sim 5 \times 10^{-6}\,M_\odot\,\mathrm{yr}^{-1}$ (Hosokawa et al. 2010). In estimating this value, a typical dust temperature of 10 K in the cold core is adopted (Zhang et al. 2022). This value during massive star formation is expected to be $\gtrsim 10^{-4}\,M_\odot\,\mathrm{yr}^{-1}$ (Hosokawa et al. 2010). Such high accretion rates support the ability of lower-mass progenitors have the ability to accrete enough material from their gas-rich circumstellar disks to grow into massive stars (e.g., Motte et al. 2018; Chen et al. 2021).

The MYSO samples were determined mainly by observational data provided by IRAS (Molinari et al. 1996) and the Midcourse Space Experiment (MSX; Hoare et al. 2005), while the Spitzer surveys of the Galactic plane using the Infrared Array Camera (IRAC, 3.6, 4.5, 5.8 and 8.0 μm; Fazio et al. 2004) that came later replaced the former with sub-2″ resolution and higher sensitivity. The Spitzer Galactic Legacy Infrared Midplane Survey Extraordinaire (GLIMPSE;

Churchwell 2001) I/II has revealed several "Extended Green Objects" (EGOs), which display extended emission in the 4.5 μm band coded as the green channel in the trichromatic image. The extended green emission is thought to be caused by MYSO outflows (Cyganowski et al. 2008; Chen et al. 2013). When the material is continually accreted from the disk to the protostar, it will release excess angular momentum and produce collimated jets or outflows (e.g., Shu et al. 1987; Hosokawa et al. 2010; Motte et al. 2018; Chen et al. 2021). The Spitzer 4.5 μm band covers excitation radiation of H_2 ($v = 0$–0, S (9, 10, 11)) and CO ($v = 1$–0) that forms in the regions of interaction between outflows and interstellar medium (Smith & Rosen 2005; Reach et al. 2006; Davis et al. 2007). The sources with extended 4.5 μm emission have a high percentage of shock-triggered masers (e.g., H_2O and CH_3OH Class I, Cyganowski et al. 2009, 2013; Chen et al. 2011; Towner et al. 2017). As the signposts of MYSOs, class II methanol masers have a high detection rate in MYSOs (Jones et al. 2020; Stecklum et al. 2021). The above evidence shows that the EGOs are excellent MYSO candidates with active outflows.

The Spitzer observation range is limited to the inner Galactic plane ($|l| < 65°$, Churchwell et al. 2009). The observation area of the Wide-field Infrared Survey Explorer (WISE) covers the entire Galactic plane (Wright et al. 2010). The exposure time of Spitzer GLIMPSE is 4 s per frame, and 5σ sensitivity is ~0.2 mJy at 4.5 μm band (Benjamin et al. 2003). The exposure time of WISE is 11 s per frame, and 5σ sensitivity is ~0.11 mJy at 4.6 μm band (Wright et al. 2010). Although WISE has an angular resolution about 3 times smaller than that of Spitzer, thanks to the long exposure time of WISE, the sensitivity of WISE is 2 times higher than that of Spitzer. In addition, the WISE data we adopted is ~1440 deg^2, which is 5 times that of Spitzer GLIMPSE (~274 deg^2). Considering sample size = (solid angle)$^*N(>S)$, where $N(>S)$ is the surface number density of sources brighter than a flux limit S, and $N(>S) \sim 1/S$, WISE is expected to find 10 times as many sources as Spitzer.

Cyganowski et al. (2008) and Chen et al. (2013) identified MYSOs by checking whether the infrared sources have extended structures. In this work, WISE W1, W2, and W3 bands are encoded as blue, green, and red, respectively, in the three-color composite images. We call sources that appear green in color or sources whose W2 is significantly larger than W1 in value as WGOs. Dense cores are localized density enhancements of the cloud material that have been recognized for sites of low- and high-mass star formation for more than 30 yr (Bergin & Tafalla 2007). WGOs, which do not show 4.6 μm extended emission, are still deeply embedded in the cores and may be at an early evolutionary stage of MYSOs. As long as there is enough gas on the envelope or disk, they have the potential to grow into MYSOs with extended structures (Jijina & Adams 1996; Yorke & Sonnhalter 2002). The ultralow temperature-cooled cameras carried by Herschel can detect far-infrared dust radiation from the dense cores (Pilbratt et al. 2010). Based on the size and mass of the core, it can be inferred whether the core can give birth to massive stars (e.g., Krumholz & McKee 2008; Kauffmann & Pillai 2010; Zhang et al. 2018). The emission of YSOs in different bands will change with the evolution process and this change is reflected in the shape of the spectral energy distribution (SED) fitting (e.g., Lada 1987; Shu et al. 1987; Andre et al. 1993; Greene et al. 1994). By fitting the SED of YSOs with the corresponding theoretical model (Robitaille 2017), we can obtain various property parameters of YSOs, such as mass, temperature, and radius. By combining these parameters, the accretion rate of YSOs can be estimated, which can predict whether YSOs can form massive stars (e.g., Jones et al. 2019; Moser et al. 2020; Stecklum et al. 2021).

The outline of the paper is as follows. In Section 2, we describe archived data used for this article. Data analysis and results are presented in Section 3. Section 4 discusses the star formation scenario of WGOs and the reliability of WGOs as MYSOs. We summarize our conclusions in Section 5.

2. Archive Data

2.1. WISE Data

WISE, equipped with a 40 cm diameter infrared telescope, performed an all-sky astronomical survey in Earth orbit over 10 months in four infrared bands, W1, W2, W3, and W4, centered at 3.4, 4.6, 12, and 22 μm wavelength (Wright et al. 2010). The angular resolutions are 6.″1, 6.″4, 6.″5, and 12.″0 respectively for wavelengths of 3.4, 4.6, 12, and 22 μm, and in unconfused regions on the ecliptic point source sensitivities at 5σ are better than 0.08, 0.11, 1, and 6 mJy. The data were released on 2012 March 14 and can be retrieved from the Infrared Science Archive.[3] We selected all the data in the range of the Galactic plane ($|b| < 2°$) covering ~1440 deg^2, including a total of ~600 small images with a size of 1.°56 × 1.°56.

2.2. Hi-GAL Data

The Herschel Infrared Galactic Plane Survey (Hi-GAL) was performed in five infrared continuum bands between 70 and 500 μm to map the dust distribution in $|b| < 1.°5$ (Molinari et al. 2010), which provide a census of dense and cold condensations that some sources may have harbored YSOs. Mège et al. (2021) resolved distances for ~80% compact sources by substituting radial velocity into the rotation of the galaxy and assisted with the H I self-absorption method or distance-extinction data to solve distance ambiguity. Based on the fitting of a modified blackbody (graybody) function to Herschel $\lambda \geqslant 160$ μm portion and the distances given by Mège et al. (2021), Elia et al. (2021) derived source physical properties, including the mass M, the temperature T, and bolometric luminosity L and so on. The source size is measured from a 250 μm wavelength image.

3. Data Analysis and Results

3.1. Identification and Classification of WGOs

We introduce a detailed process for screening WGOs in this section. We first divide the W2 image by the W1 image pixel by pixel, pixels with an intensity ratio greater than 1.7 are retained, and those less than 1.7 are discarded, after that, sources with a size $\gtrsim$ one beam (6″ × 6″) were extracted as "Raw Sample." Then, we matched the "Raw Sample" and ALLWISE source catalog (Wright et al. 2019) within 6″ and obtained 17311 "WISE Associations." YSOs with thick accretion disks usually radiate significantly in the 12 or 22 μm and can be detected even at substantial distances (Wright et al. 2010). So we further selected the samples with emission in the 12 or 22 μm to ensure that they are YSOs in an

[3] https://irsa.ipac.caltech.edu/Missions/wise.html

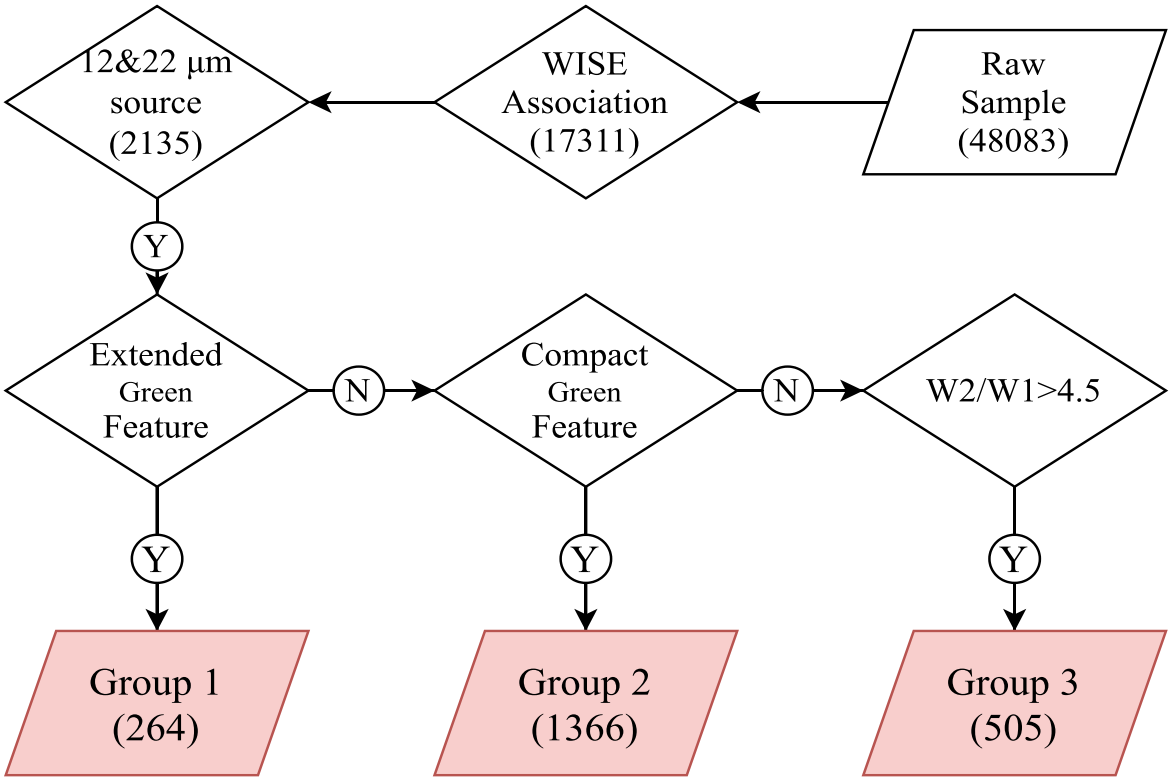

Figure 1. Flow chart describing the identification procedure of WGOs.

early accretion stage. In addition, based on our investigation, the ratio of W2 and W1 of most (over 80%) identified EGOs in WISE is greater than 4.5. So according to this feature, if the ratio of the intensity of the 4.6 μm band to the intensity of the 3.4 μm band is more significant than 4.5, such a source we also temporarily consider as WGOs. WGOs cannot be directly identified by the ratio of the 4.6–3.4 μm band alone, and this feature also appears in the late stages of some stellar evolution, such as asymptotic giant branch (AGB) stars (Busso et al. 1999; Herwig 2005), which makes us confuse them with WGOs. Therefore, we rule out possible targets in Table 1 from WGOs candidates with nongreen features by cross-identifications with the SIMBAD database in 6″ (WISE approximate resolutions at 3.4, 4.6, and 12 μm), which contains valuable object type information of our targets (Wenger et al. 2000). Figure 1 is a flow chart for identifying WGOs and the final number of the WGOs is 2135.

To effectively identify the extended or compact green objects, we displayed a WISE three-color image in about 2.43 deg^2 ($1\overset{\circ}{.}56 \times 1\overset{\circ}{.}56$) mosaics, in which 3.4 μm (W1) band for blue channel, 4.6 μm (W2) band for the green channel, 8.0 μm (W3) band for the red channel. In addition, images of W2/W1 in the same format as the three-color images were also made to search for WGOs that were not green. Each image was independently visually searched twice by the three authors of this paper, and only WGOs approved by all three were added to the catalog. All WGOs are divided into three subcatalogs according to morphological features and the intensity ratio of W2 and W1 (Figure 1). Extended green structure is an obvious external feature of MYSO. WGOs with extended green structures are classified as Group 1, with detailed selection criteria being that the ratio of the major axis to the minor axis of the source is $\gtrsim$1.2. WGOs with green compact morphology but without extended structure are classified into Group 2. Group 3 has no apparent green color feature, but its intensity ratio of W2 and W1 is more significant than 4.5. Figure 2 shows an example of the WGOs in Groups 1, 2, and 3. Since groups 2 and 3 do not yet have extended structures formed by outflow activity, they may be younger than traditional EGOs and may be MYSO candidates at an early stage. The number of groups 1, 2, and 3 are 264, 1366, and 505, accounting for 12%, 64%, and 24% of the total.

Table 1
Objects in SIMBAD Used to Rule Out Possible Evolved Targets

Object Type in SIMBAD	Object Type in SIMBAD
Star	Nova
OH/IR star	Post-AGB star
Carbon star	Nova-like star
Variable star	Mira candidate
Wolf–Rayet star	Planetary nebula
Emission-line star	AGB star candidate
Possible carbon star	Post-AGB star candidate
Long-period variable star	Possible planetary nebula
Variable star of RR Lyr type	Variable star of Mira Cet type
Asymptotic giant branch (AGB) star	

3.2. Galactic Distribution of the WGOs

2135 WGOs are shown in Figure 3(a). 1578 WGOs are in $|l| < 60°$, which make up 74% of the total sample. WGOs in $|l| < 60°$ are not symmetrically distributed. 709 WGOs locate in the range of [0°, 60°] with a peak at ∼15°. 869 WGOs locate in [−60°, 0°] with a peak at ∼25°. The number in [−60°, 0°] is 20% more than that in [0°, 60°]. 556 WGOs are in $|l| > 60°$. WGOs are mainly distributed in $75° < l < 85°$, 105°

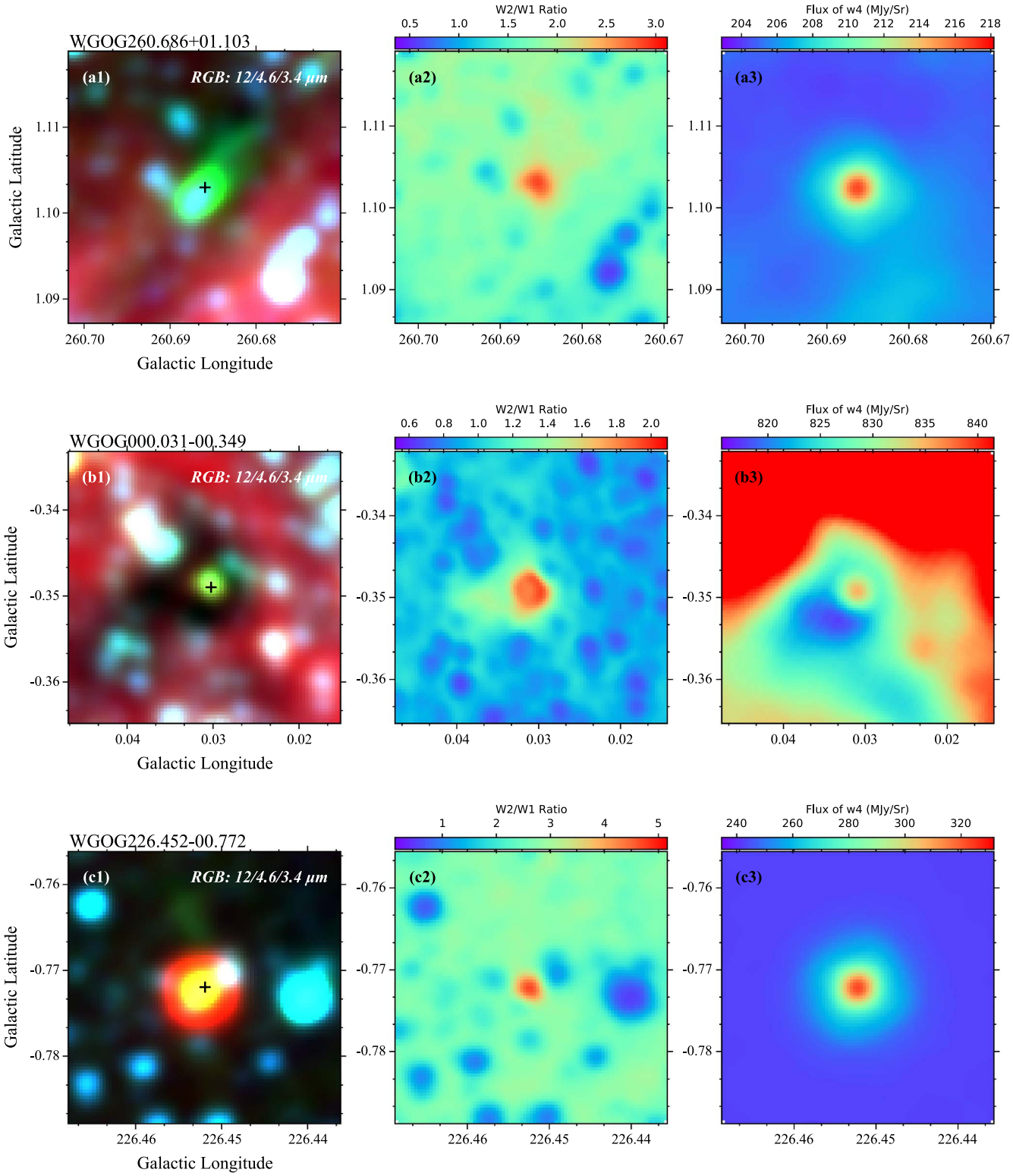

Figure 2. Morphology of the exemplary WGOs. Panels (a), (b), and (c) represent groups 1, 2, and 3. Panels (a1), (b1), and (c1) are trichromatic maps of emission at 3.4, 4.6, and 12 μm, rendered in blue, green, and red. Panels (a2), (b2), and (c2) are W2/W1 ratio maps. Panels (a3), (b3), and (c3) show 22 μm images. The black cross marks the center of each WGO.

$< l < 115°$, $130° < l < 135°$, $-105° < l < -95°$ and $-155° < l < -135°$ regions, which are coincident with the locations of the Cygnus, Cepheus, Cassiopeia, Vela, and Monoceros giant molecular clouds respectively.

As the parent structure of the YSO, the size and mass of the Hi-GAL compact source determine the potential to form the massive star. We crossmatched WGOs and Hi-GAL compact source catalog and found 1260 WGOs have Hi-GAL source counterparts. Among them, 1151 sources have complete information from Elia et al. (2021), such as heliocentric distance, luminosity, mass, and temperature. We adopt the distance of the Hi-GAL sources as the distance of the

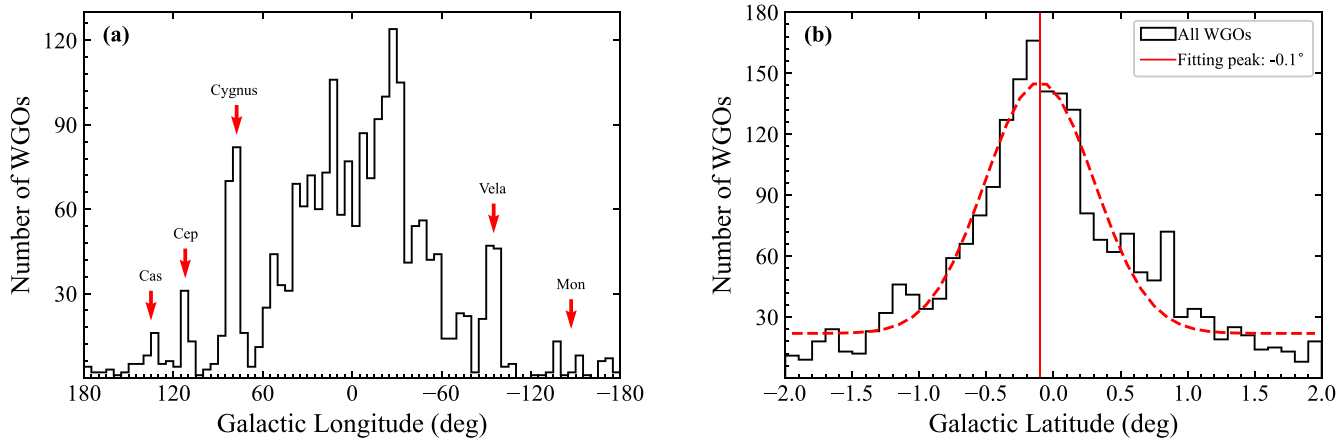

Figure 3. Panel (a) is the number distribution of WGOs as a function of Galactic longitude in 5° bins. The locations of giant molecular clouds are indicated by red arrows. Panel (b) shows the number distribution of WGOs as a function of Galactic latitude in 0.°1 bins and fitted with a Gaussian curve. The red vertical line denotes the peak position of the Gaussian curve.

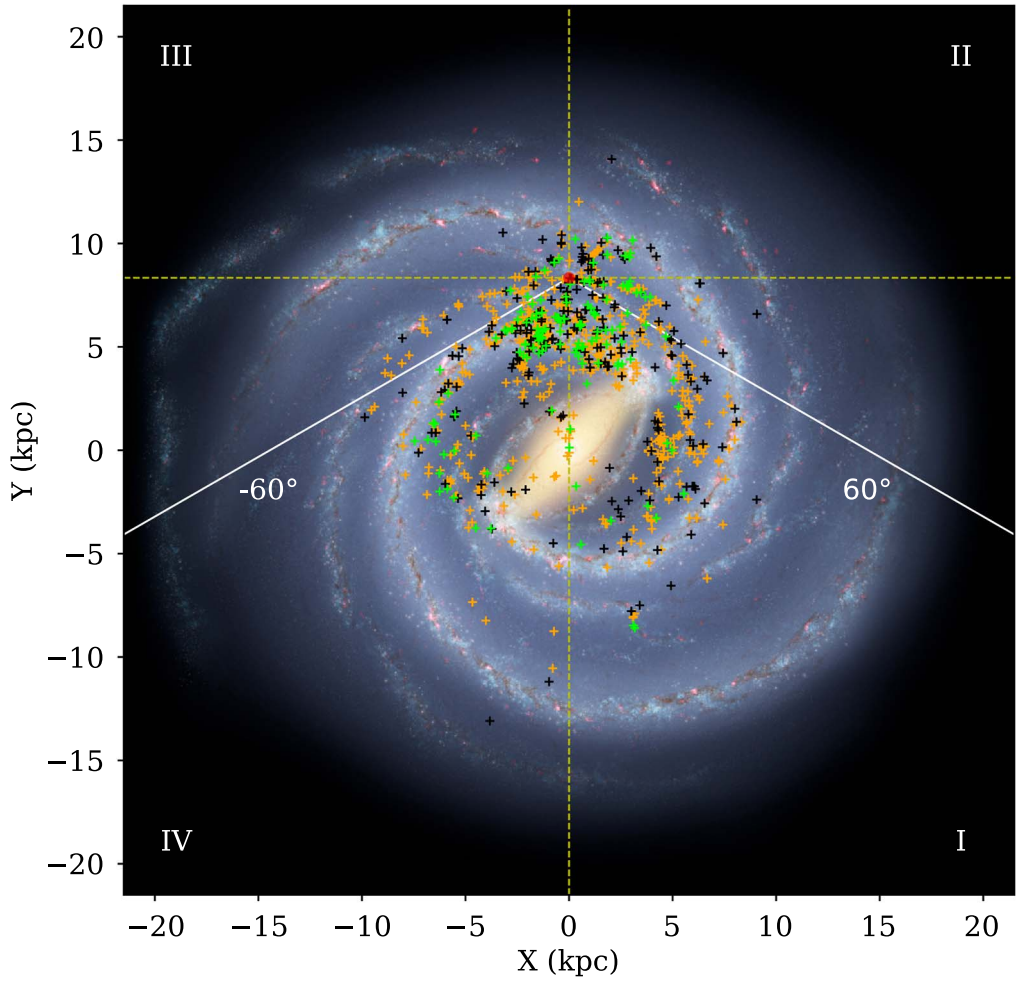

Figure 4. The distribution of WGOs in the Galactocentric system. The axes are Galactocentric distances. We mark the WGOs of three different groups with green, yellow, and black crosses, respectively. The background image is a sketch of the galaxy produced by Robert Hurt (artist's concept, R. Hurt: NASA/JPL-Caltech/SSC). The position of the Sun is shown by the red circle above the Galactic midplane. The two solid white lines enclose the inner Galactic plane ($|l| < 60°$).

corresponding WGOs. Figure 4 gives an overview of the distribution of those 1151 WGOs in the Milky Way viewed from the north Galactic pole. If we only infer the distribution of WGOs from Figure 3, an erroneous conclusion will be obtained, that WGOs are concentrated in the Galactic Center, because the projection effect is not considered. But in Figure 4 we can see that most of the WGOs are distributed along the spiral arm. Many WGOs in the line-of-sight direction are just projected to the CMZ, but the actual distance is not that far.

The red dashed line in Figure 3(b) shows the distribution of WGOs on the Galactic latitude ($|b| < 2°$), which can be well

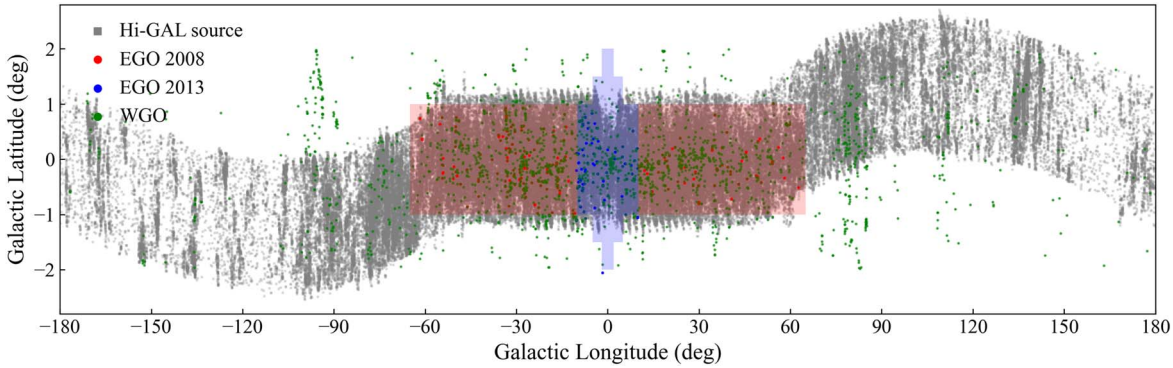

Figure 5. Distribution of WGOs, EGOs, and Hi-GAL sources in the Galactic plane. Green circles represent WGOs; red and blue circles represent EGOs identified by Cyganowski et al. (2008) and Chen et al. (2013) respectively. The gray points show the Hi-GAL compact sources (Elia et al. 2021). The coverage of GLIMPSE I and II surveys are shaded in red and blue, respectively.

fitted with a Gaussian curve, with FWHM of 1° and a peak of ∼150. In the FWHM range (±1°) of this Gaussian curve, the number of WGOs accounts for 80% of the total sample. The center position of this Gaussian curve is not at the center of the Galactic coordinates but shifted to the left by 0.°1 (see the red vertical line in Figure 3(b)). This small offset also exists in the distribution of the core or clump structures such as the ATLASGAL survey (Schuller et al. 2009) and the Hi-GAL survey, with a negative peak of latitude ($b = -0.°05$ and $-0.°09$ respectively). This may be because our solar system is slightly above the Galactic plane, and the viewing line of sight causes this offset (Schuller et al. 2009), but Hinz et al. (2009) argue that there are more molecular clouds in positive longitude, obscuring the dense source that results in this offset.

3.3. Crossmatch with Previous Catalogs

Using Spitzer survey data, Cyganowski et al. (2008) cataloged ∼300 EGOs and Chen et al. (2013) cataloged 98 EGOs. There are 1401 WGOs in the GLIMPSE I and II survey region (see red and blue regions in Figure 5). Identification of EGO relies on visual inspection of objects in the Spitzer three-color images for the presence of green and extended structures. The identification methods of WGOs are similar to that of EGOs, both are visual inspection, but our adopted sample also includes the compact green sources and the sources with excess emission $W2/W1 \gtrsim 4.5$. We crossmatched our WGOs to Spitzer EGOs within 6″, which is equivalent to the resolution of WISE 3.4 and 4.6 μm bands, and found 70, 97, and 41 WGOs in each group are previously discovered EGOs. About half of EGOs do not have a corresponding WGO. After viewing blow-up images for each band of WISE of those unmatched EGOs, we found that the main reason why these EGOs were not picked from the WISE data was the lack of flux in the W3 or W4 bands, which accounted for more than 76% of the EGOs, and the remaining EGOs whose W2/W1 ratio failed to exceed our threshold of 1.7. There is no case where the source blends with adjacent targets due to the low resolution of the WISE and is not recognized.

Due to the constraint of the (approximately $|b| < 1.°5$) survey range of Hi-GAL (Molinari et al. 2010), 363 WGOs are distributed outside this range, and about 71% (1260/1772) of WGOs have Hi-GAL counterparts within this range. By observing the positions of the remaining nearly 30% WGOs in the survey range (see the gray points in Figure 5), we found that some of them are located at the edge of the observation field and therefore cannot be effectively identified as sources. However, due to the lack of dust emission, the possibility of a few objects in WGOs unrelated to star formation cannot be ruled out. This needs to be further confirmed by follow-up observations. About 36% of the Hi-GAL sources are less than 0.1 pc in size which is the core scale, and the sizes of the remaining 64% are between 0.1 and 1 pc at the clump scale. The median values of the luminosity, mass, and distance are 771 $L_\odot$, 320.6 $M_\odot$, and 3.7 kpc, respectively. We also crossmatched the ATLASGAL YSOs catalog (Urquhart et al. 2022) in the inner Galactic plane ($|l| < 60°$) without $|l| < 3°$, and we found that 1176 WGOs cannot match ATLASGAL YSOs.

Kuhn et al. (2021) presented a catalog of $\sim 1.2 \times 10^5$ YSOs based on the Spitzer/IRAS survey (the inner Galactic plane, approximately $-105° < l < 110°$, $|b| < 2°$). 1992 WGOs located at this survey coverage area, and 1095 WGOs match YSOs within 6″. The match rate is 54.9%. Marton et al. (2016) identified over 13300 YSOs using 2MASS and WISE photometric data combined with support vector machine in all sky. Our WGOs show a low match ratio with this catalog, with only 68 WGOs can match. Meanwhile, the Red MSX Source (RMS) survey (Lumsden et al. 2013) provided a catalog with nearly 2800 YSOs, which included 115 MYSOs. 1859 WGOs locate in the range of the RMS catalog ($10° < l < 350°$), and we found that 1653 WGOs are newly identified.

3.4. Crossmatch with Masers of the Star Formation Indicators

In the early stage of star formation, MYSOs are deeply embedded within dense molecular cores, with a short accretion period, and remain in the core for a long time even after entering the main-sequence phase. Fortunately, large-scale or unique molecular emissions triggered by massive star formation, such as masers, can help identify them (Beuther et al. 2007). We crossmatched WGOs with five masers (CH_3OH Class I/II, H_2O, SiO, and OH) related to star formation, using the online tool *MaserDB*,[4] provided by Ladeyschikov et al. (2019). Since different distances of WGOs will have a considerable impact on the actual matching radius, and the information on them is incomplete, so we use a uniform matching angular radius that is a WISE resolution of 6″, which corresponds to ∼0.15 pc at WGOs mean distance of 5.17 kpc and close to a typical core size (0.1 pc, Zhang et al. 2022).

[4] https://maserdb.net/

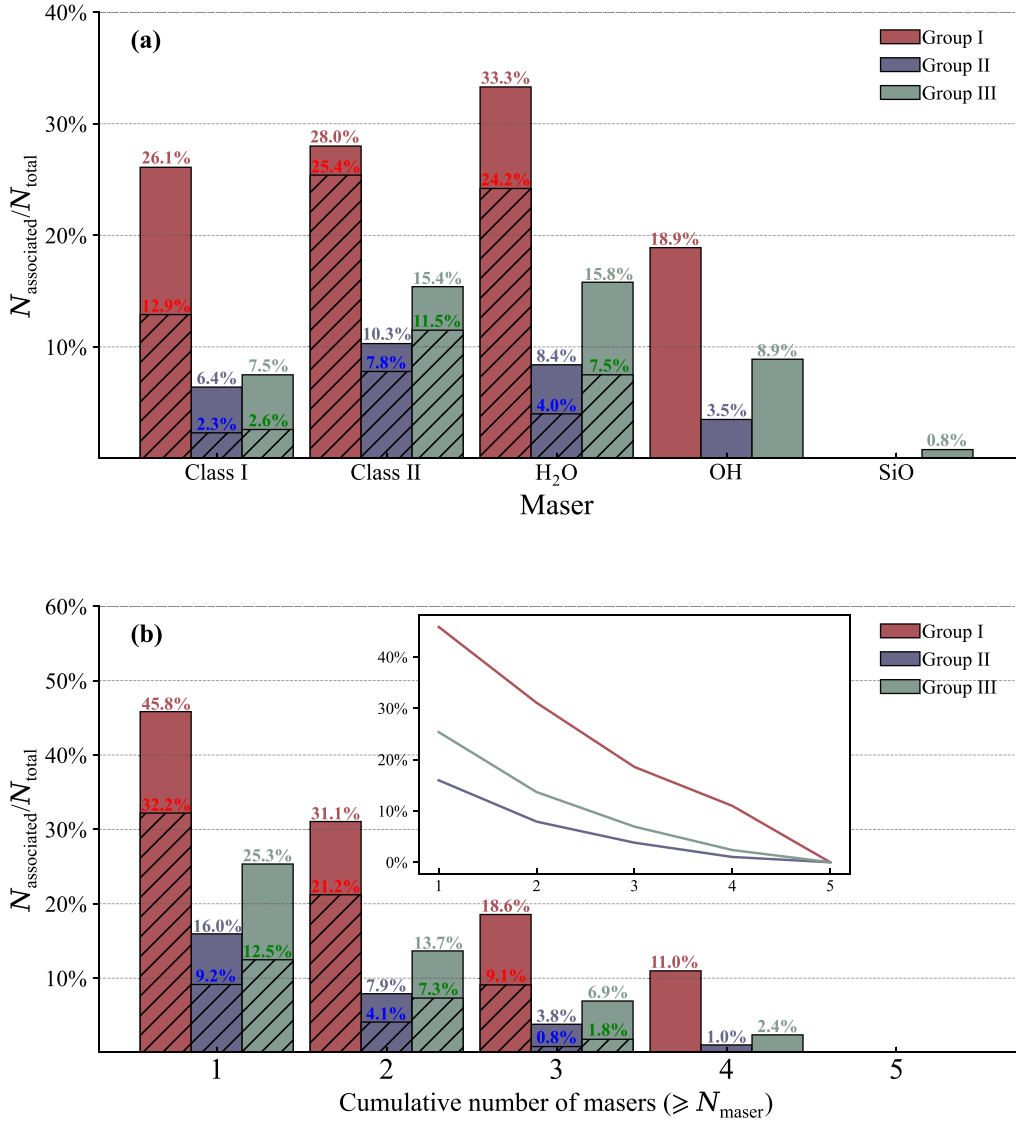

Figure 6. The association rate of the WGOs in each group with five kinds of masers (methanol Class I/II, H_2O, OH, and SiO; upper panel). $N_{associated}$ is the number of the WGOs associated with the maser. N_{total} is the total number of WGOs in each group. The red, blue, and green bars represent Groups 1, 2, and 3 respectively. The lower panel is the association rate of WGOs with the cumulative number of masers ($\geqslant N_{fig6}$). $N_{associated}$ in this panel is the number of WGOs associated with at least N_{fig6} masers. The inset in panel (b) shows the change of association rate between each group of WGOs and the cumulative number of masers.

Masers detected by single-dish and interferometric observations have been selected separately. We separately counted the association rate of the WGOs in each group with five kinds of masers and the association rate of WGOs with the cumulative number of masers, which are shown in Figures 6(a) and (b), respectively. *MaserDB* distinguishes the interferometric positions of methanol Class I/II, H_2O masers from their single-dish positions, but no interferometric positions for OH and SiO masers are provided. Each bar in Figure 6 shows the association rate of all maser data, including interferometric and single-dish data, and the slash-covered portion of each bar shows the associated rate of only interferometric maser data. In Figure 6(a), the shapes of bars in every kind of maser, except SiO, are similar, whether it is all maser data or only interferometric data. The most ubiquitous type of masers is water, as it is associated with different astronomical objects (Furuya et al. 2003; Szymczak et al. 2005), at different stages of evolution (e.g., protostellar jets, Hollenbach et al. 2013; large-scale shocks, Mac Low et al. 1994; disks, Gallimore et al. 2003). It is also consistent with the statistical results shown in Figure 6(a). While methanol masers are less ubiquitous. The inset in Figure 6(b) more intuitively shows the change of association rate between each group of WGOs and the cumulative number of masers. Statistics based on Figure 6 show that maser association rates in Group 1 are at least 3 and 2 times greater than Groups 2 and 3, and Group 3 is slightly higher than Group 2.

3.5. Derived Physical Parameters of the WGOs from the SED Models

We constructed SEDs with WISE four and Herschel five wavelengths ranging from 3.4 to 500 μm for 1151 WGOs with Hi-GAL source counterparts. Robitaille (2017) provided 18 kinds of model sets, each containing 10,000 models for fitting YSOs in different evolution stages. Based on the prior knowledge of WGOs, there are possibly embedded protostars with an accretion disk or outflow. The model sets we selected

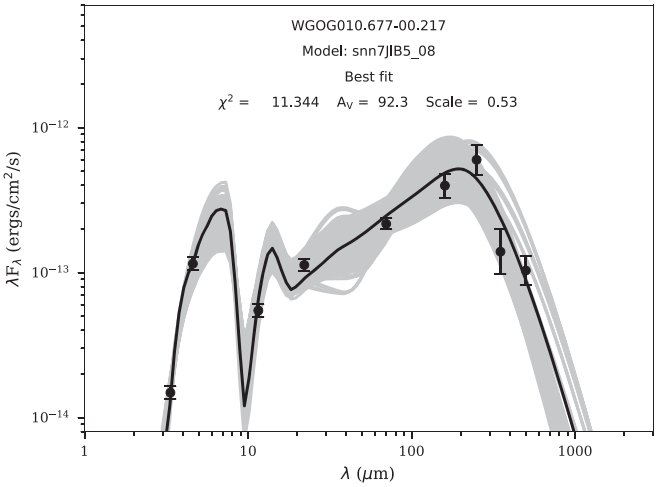

Figure 7. An example of SED fitting. Photometric data from WISE and Hi-GAL were fitted using the YSO models of Robitaille (2017). Black and gray lines represent the best fit and good fit that satisfy $\chi^2-\chi^2_{\rm best} < 3N_{\rm data}$, where $N_{\rm data}$ is the number of data points. The $P(D|M)$ score of this fitting is 4.564.

are s-smi, sp-smi, sp-hmi, s-p-smi, s-p-hmi, s-pbsmi, s-pbhmi, s-u-smi, s-u-hmi, s-ubsmi, s-ubhmi, spu-smi, and spu-hmi. All 13 model sets contain one or more features, such as envelope or accretion disk or outflow. Fitting the SED of each WGO to the 13 different model sets return χ^2 for each model set. We used $\chi^2-\chi^2_{\rm best} < 3N_{\rm data}$ as a criterion to select good fits from all model sets. Robitaille (2017) suggested using a Bayesian approach to compare how well different model sets explain a set of data. $P(D|M) \propto N_{\rm good}/N$, where $N_{\rm good}$ is the number of good models from a given model set, and N is the total number of models in that set, is used to indicate the reliability of the model set to the data. In this way, for each WGO, we only need to compare 13 different values of $P(D|M)$, and the highest value of $P(D|M)$ represents the most suitable model set. We show an example of SED fitting in Figure 7. Based on the fitting results of the best model set for each WGO, we calculated the mean stellar radius $R_\star$ and surface temperature $T_{\rm eff}$, weighted by $1/\chi^2$. The uncertainties of $R_\star$ and $T_{\rm eff}$ are from weighted standard deviations (e.g., Towner et al. 2019; Chen et al. 2021).

The YSO total luminosity is composed of photospheric luminosity ($L_\star$) and accretion luminosity ($L_{\rm acc}$; e.g., Chen et al. 2021; Hunter et al. 2021; Olivier et al. 2021)

$$L_{\rm tot} = L_\star + L_{\rm acc}. \quad (1)$$

Here we assume all YSOs are absolute blackbodies and spherical. According to the Stefan–Boltzmann law, the stellar luminosity $L_\star$ can be derived.

The median values of $L_\star$ in each group of WGOs are 16.6 $L_\odot$, 5.4 $L_\odot$, and 7.4 $L_\odot$ respectively. The median value of $L_\star$ in Group 1 is much larger, perhaps indicating that WGOs in Group 1 are more mature than the other two groups. The accretion rate $\dot{M}_{\rm acc}$ can be estimated from accretion luminosity (Zhang & Tan 2011)

$$L_{\rm acc} = \frac{GM_\star \dot{M}_{\rm acc}}{R_\star}, \quad (2)$$

where G and $M_\star$ are the gravitational constant and mass of the protostar. $M_\star$ is calculated according to the method proposed by Tout et al. (1996). The mean $M_\star$ of each group are 2.6 ± 1.6 $M_\odot$, 1.9 ± 0.9 $M_\odot$, and 2.3 ± 1.5 $M_\odot$ respectively. The Hi-GAL source is the parent structure of the protostars, which wraps the protostars, and its luminosity can be regarded as the total luminosity of the protostars. It should be noted that protostars are embedded in cores or clusters, and multiple protostars may be accreting simultaneously (Smith et al. 2009; Cyganowski et al. 2017), but massive protostars are usually much more luminous than low-mass protostars. On the contrary, low-mass protostars contribute little to luminosity. We obtained the median values of $\dot{M}_{\rm acc}$ of each group are $2.04 \times 10^{-4}\,M_\odot\,{\rm yr}^{-1}$, $2.91 \times 10^{-5}\,M_\odot\,{\rm yr}^{-1}$, and $4.22 \times 10^{-5}\,M_\odot\,{\rm yr}^{-1}$, respectively.

4. Discussion

4.1. The Star Formation Scenario of the WGOs

Whether a source can be successfully detected depends on its intensity in the direction of sight. 4.5 μm emission of the EGOs identified by Cyganowski et al. (2008) is $\gtrsim$4 MJy sr^{-1}, and the flux intensity of most of the EGOs in the Spitzer 4.5 μm band is significantly higher than that in the 3.6 μm band (Noriega-Crespo et al. 2004; Cyganowski et al. 2008). We screened 2135 WGOs as young candidates for massive stars, significantly outnumbering Spitzer EGOs, which benefits from WISE being twice as sensitive as Spitzer (Benjamin et al. 2003; Wright et al. 2010), even though they are filtered by multiple thresholds we set. The empirical relationship between the star formation rate (SFR) in our galaxy and the physical properties of interstellar gas is known as Kennicutt–Schmidt law: $\Sigma_{\rm SFR} \propto \Sigma^N_{\rm gas}$. This relation states that the SFR is positively related to gas density with the index of the power law being $\sim$2 in the solar neighborhood (Schmidt 1959) and 1.4 in a larger set of galaxies (Kennicutt & Evans 2012). Cold dust view reveals the confined dust lane in the Galactic plane, which is bright at $-48° < l < 40°$, but outside this range gets weaker significantly (Csengeri et al. 2016). WGOs are mainly distributed in $|l| < 60°$, which are synergistic with the gas in the plane of the Milky Way. The central molecular zone (CMZ, the inner $\pm 1.^\circ 5 \times \pm 0.^\circ 5$ around the Galactic center) contains $\sim$10% of the neutral gas of the galaxy ($\sim$5–10 $\times$ $10^7\,M_\odot$; Barnes et al. 2017), but only accounts for 0.1% of the surface area. CMZ has a large amount of dense molecular gas; however, due to the extreme environment in this region, its star formation efficiency is very low, only $\sim$0.07–0.15 $M_\odot\,{\rm yr}^{-1}$ (Crocker et al. 2011; Yusef-Zadeh et al. 2009; An et al. 2011). At the same time, it lacks YSOs with high mass and low mass (the total mass of YSOs in the CMZ is $\sim 7.7 \times 10^4\,M_\odot$; Immer et al. 2012). The number of our WGO samples is lacking in the CMZ, which is consistent with the low SFR in this region.

According to the classification method of the WGOs, Group 1 WGOs are most in line with the morphological characteristics of traditional EGOs (Cyganowski et al. 2008; Chen et al. 2013). The Group 2 WGOs lack extended structures but show compact green features. The Group 3 WGOs have neither extended structure nor green features, but W2 is 4.5 times larger than W1. The resolution of WISE is about three times lower than that of Spitzer, so extended structures of some WGOs may be not identified and are classified into Group 2 or 3. WGOs in Groups 2 and 3 do not exhibit extended structures, they show relatively strong W2 band emissions and are usually surrounded by dense gas, and they may be in an earlier stage (e.g., Class I even Class 0 of YSO, Bachiller 1996; Shu et al. 1987) than the Group 1 and are currently accreting gas.

Molecular tracers behave differently through the evolutionary sequence, and the late evolutionary sequence may contain more complex molecular tracers (Sanhueza et al. 2012). Different masers usually indicate different evolution stages of YSOs, and the star-forming regions with later evolution stages show more complex maser components (e.g., Wang et al. 2011). Class I methanol masers excited by the shock waves are usually found at some distance from a radiation source (Sobolev et al. 2007). It is worth noting that it may occur at the earliest stage, earlier than all masers (Cragg et al. 1992; Ellingsen 2006). Class II methanol masers are widely considered to be some of the most reliable tracers in the early stage of high-mass star formation (Ellingsen 2006, and references therein), and these masers are only related to high-mass star formation activities (Breen et al. 2013). We speculate that the WGOs of Group 1 are in the latest evolutionary stage compared to the other two groups, and the shock wave excited by the strong star formation activity that even excited them near the radiation source leads to the highest association rate with Class I maser near the radiation source. The inference about the evolution stage of Group 1 can also be deduced by observing the association rate of the OH maser: the OH maser is a sensitive tracer of ultracompact H II (UC HII) region (Reid 2002), and the occurred of UC H II region indicates a later stage of star formation. Several previous studies have shown that water maser in star-forming regions can be excited by a variety of star-forming activities (e.g., Mac Low et al. 1994; Gallimore et al. 2003; Hollenbach et al. 2013), and it is obvious that various activities occurring with the process of evolution will improve the excitation rate of water master. The SiO maser has been known associated with late-type stars, such as stars on the AGB (Matsuura et al. 2000; Nakashima & Deguchi 2000). The SiO maser was confirmed that it in star-forming regions is a rare phenomenon by Zapata et al. (2009) as it was only detected from known regions (e.g., Orion KL, Snyder & Buhl 1974; W51 North, Sgr B2, Hasegawa et al. 1986; Sgr B2(N), Higuchi et al. 2015; G19.61-0.23 and G75.78 +0.34, Cho et al. 2016). This also leads to the fact that in Figure 6(a), the SiO maser appears to be almost unassociated with any WGOs.

4.2. How Many WGOs Are Highly Reliable MYSOs?

The extended structure of the EGOs is likely to be related to the molecular outflow resulting from the shock emission from the molecules H_2 and CO during the formation of a massive star (Cyganowski et al. 2008; Chen et al. 2013). The WISE 4.6 μm is very close to Spitzer's 4.5 μm, and we believe that the extended structure traced by WISE 4.6 μm is also due to the outflow. Outflow is observed toward both low-mass (e.g., the famous well-researched Herbig–Haro object HH46/47, Noriega-Crespo et al. 2004; Velusamy et al. 2007) and high-mass sources. Strong outflow is one feature of MYSOs. Compared to the flux rate of low-mass outflow $\sim 10^{-6}\,M_\odot\,\mathrm{yr}^{-1}$, the flux rate of MYSOs can be stronger than $10^{-3}\,M_\odot\,\mathrm{yr}^{-1}$ (Arce et al. 2007). The bright emission in the W2 may be a precursor to a strong outflow in future evolutions. However, it cannot be ruled out that there is not enough gas in the parent structure to provide enough gas for it to evolve into a massive star. Thanks to the multiband SED models for YSOs, we can predict the evolution of the sources and provide us with a way to get more believable subsamples (Robitaille et al. 2006; Robitaille 2017). Massive stars form in clusters (Lada & Lada 2003; Kruijssen 2012), and there may be multiple YSOs for one WGO (e.g., MM1 ∼ 19 in EGO11.92-0.61, Cyganowski et al. 2017). Limited by the resolution of the WISE, it is indistinguishable. But the massive YSOs have a strong gravitational advantage that will limit the mass of other YSOs in the cluster, once formed, would dissipate the natal cloud, preventing further star formation (e.g., Herbig 1962). Meanwhile, the luminosity and accretion rate of the massive YSOs are far higher than those of other low-mass YSOs (Arce et al. 2007; Hosokawa et al. 2010).

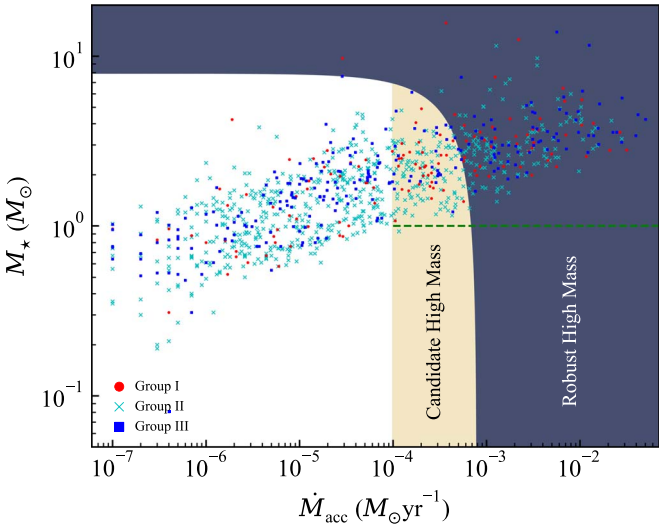

Figure 8. Accretion rate versus protostellar mass. Red circles, blue squares, and cyan crosses represent WGOs in groups 1, 2, and 3, respectively. The WGOs listed in Tables 2 and 3 are located in the deep blue and light yellow areas, respectively. The green dotted line marks the mass equal to 1 $M_\odot$, and almost all MYSO candidates are above this line.

We selected the WGOs with $M_\star + \dot{M}_{\rm acc} \times 10^4\ \mathrm{yr} > 8\ M_\odot$ (see the blue area in Figure 8) as robust MYSO candidates, which are listed in Table 2 and the numbers in each group are 46, 118, and 67. The accretion rate changes dramatically during massive star formation, but considering the accretion timescale is usually shorter than 10^4 yr, it is generally believed that the accretion rate of MYSOs is $\sim 10^{-4}$–$10^{-3}\,M_\odot\,\mathrm{yr}^{-1}$ (Zhang & Tan 2011). We selected WGOs with $\dot{M}_{\rm acc} > 10^{-4}\ M_\odot\ \mathrm{yr}^{-1}$ (see the yellow area in Figure 8) as candidate MYSOs. Table 3 lists those candidate MYSOs. The numbers in each group are 32, 110, and 30. 63% WGOs in Group 1 are robust or candidate MYSOs, much higher than the ratio in Groups 2 and 3 (34% and 40%). This probably implies that the WGOs in Group 1 have the greatest potential to form massive stars. By observing Figure 8, we found that almost all stellar masses of MYSO candidates are higher than 1 $M_\odot$. Based on the relation of masses and radii of the Hi-GAL sources, we inferred whether massive stars would form. Prestellar and starless cores are separated by the three dotted green lines $\Sigma_{\rm crit} = 0.024\ \mathrm{g\,cm}^{-2}$ (Lada et al. 2010), $\Sigma_{\rm crit} = 0.027\ \mathrm{g\,cm}^{-2}$ (Heiderman et al. 2010) and $M(r) = 460\,M_\odot (r/\mathrm{pc})^{1.9}$ (Larson 1981) in Figure 9, and the green area means the core in which is not bound by gravity may disperse after a period of time, so the probability of forming stars is very low. Only a few WGOs' Hi-GAL source counterparts are under this line, therefore, we can infer that most WGOs' Hi-GAL source counterparts can produce star-forming activity. The upper shaded region in Figure 9 indicates the parameter space of massive protoclusters, defined by Bressert et al. (2012), where there is almost no WGO

Table 2
Robust MYSOs

Name	Group	l	b	Model Set	Stellar Mass (M_*)	Accretion Rate ($\dot{M}_{\rm acc}$)	Distance	$\geqslant 870\,M_\odot R^{1.33}$	$\geqslant 1$ g cm^{-2}	Class II Methanol Maser
		(deg)	(deg)		$M_\odot$	$\times 10^{-4}\,M_\odot$ yr^{-1}	(kpc)			
(1)	(2)	(3)	(4)	(5)	(6)	(7)	(8)	(9)	(10)	(11)
G000.091-00.663	I	0.0912	−0.6628	s-ubsmi	3.17(0.48)	6.073	8.21	✓	✓	✓
G000.484-00.700	I	0.4837	−0.7003	s-u-smi	15.72(4.83)	3.684	7.32	✓	✓	
G002.529+00.199	I	2.529	0.199	s-u-hmi	3.71(0.04)	31.305	12.91	✓	✓	
G004.827+00.231	I	4.827	0.2306	s-pbhmi	2.23(0.0)	55.936	3.62	✓	✓	
G006.797-00.258	I	6.7968	−0.2581	s-ubsmi	2.56(0.21)	116.692	3.82	✓	✓	✓
G009.779-00.167	I	9.7785	−0.1672	s-u-smi	4.28(3.82)	17.838	11.92	✓		
G010.628-00.337	I	10.6281	−0.3369	s-ubhmi	5.43(4.24)	68.455	17.23	✓		

Note. Column (1): source name (Galactic coordinates); column (2): a group of WGOs; columns (3) and (4): position (l and b, respectively) of the brightest 4.6 μm emission associated with the WGO; column (5): name of the best-fit model set for each WGOs; column (6): protostellar mass obtained from Tout et al. (1996), the uncertainty in brackets is obtained by propagation of uncertainty; column (7): accretion rate obtained from SED fitting (Robitaille 2017); column (8): distance of WGO from Elia et al. (2021); columns (9) and (10): thresholds, which indicate whether the source can form massive stars, and high-mass sources are marked with ✓; column (11): Class II methanol maser, and if the source is associated with it, then marked with ✓.

(This table is available in its entirety in machine-readable form.)

Table 3
Candidate MYSOs

Name	Group	l	b	Model Set	Stellar Mass ($M_\star$)	Accretion Rate ($\dot{M}_{\rm acc}$)	Distance	$\geqslant 870\, M_\odot R^{1.33}$	$\geqslant 1$ g cm^{-2}	Class II Methanol Maser
		(deg)	(deg)		$M_\odot$	$\times 10^{-4}\, M_\odot$ yr^{-1}	(kpc)			
(1)	(2)	(3)	(4)	(5)	(6)	(7)	(8)	(9)	(10)	(11)
G001.934-00.170	I	1.9344	−0.1699	s-pbhmi	2.61(0.12)	3.256	10.09	✓		
G008.683-00.368	I	8.6833	−0.3678	s-u-hmi	3.11(0.0)	1.89	4.19	✓	✓	✓
G010.477-00.358	I	10.4768	−0.3584	s-u-smi	1.39(0.53)	5.681	17.1	✓	✓	
G011.918-00.613	I	11.9181	−0.6131	s-smi	3.06(1.44)	1.243	3.4	✓	✓	
G012.683-00.183	I	12.6827	−0.1829	s-pbsmi	2.72(1.73)	1.507	2.4	✓	✓	✓
G012.890+00.491	I	12.8904	0.4915	s-pbhmi	1.76(0.31)	1.904	2.3	✓	✓	✓
G028.832-00.252	I	28.832	−0.2522	s-u-smi	3.17(0.32)	4.383	4.86	✓	✓	✓

Note. Column (1): source name (Galactic coordinates); column (2): a group of WGOs; columns (3) and (4): position (l and b, respectively) of the brightest 4.6 μm emission associated with the WGO; column (5): name of the best-fit model set for each WGOs; column (6): protostellar mass obtained from Tout et al. (1996), the uncertainty in brackets is obtained by propagation of uncertainty; column (7): accretion rate obtained from SED fitting (Robitaille 2017); column (8): distance of WGO from Elia et al. (2021); columns (9) and (10): thresholds, which indicate whether the source can form massive stars, and high-mass sources are marked with ✓; column (11): Class II methanol maser, and if the source is associated with it, then marked with ✓.

(This table is available in its entirety in machine-readable form.)

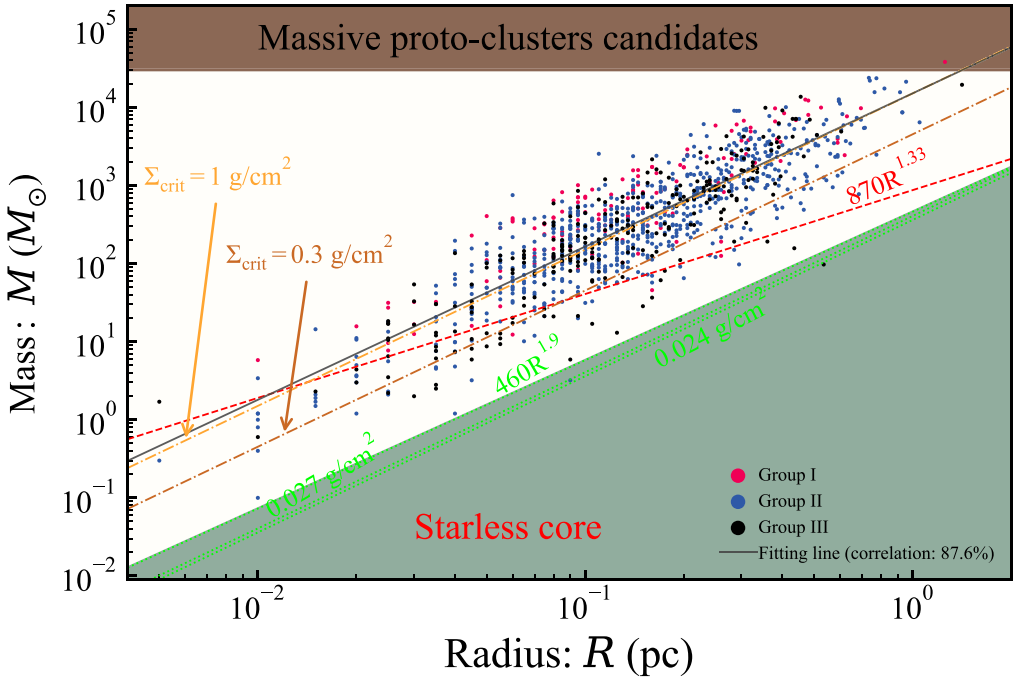

Figure 9. Mass and radius diagram of Hi-GAL compact sources corresponding to WGOs in each group. The black solid line shows a clear correlation between source radius and mass, $\log_{10}(M/M_\odot) = 1.96\log_{10}(R/\mathrm{pc}) + 4.18$. The red dashed line shows the sources which may form a high-mass star. The yellow dashed–dotted line indicates another higher threshold ($\Sigma_{crit} = 1\mathrm{g\ cm^{-2}}$) for judging high-mass clumps. The deep yellow dashed–dotted line shows a lower threshold than the yellow one.

distribution. Based on theoretical arguments, Krumholz & McKee (2008) established a critical value of $\Sigma_{crit} = 1\ \mathrm{g\ cm^{-2}}$ ($M(r) = \pi\Sigma_{crit}r^2$, dashed–dotted yellow line in Figure 9), but Butler & Tan (2012) and López-Sepulcre et al. (2010) obtained a smaller value of $\Sigma_{crit} = 0.3\ \mathrm{g\ cm^{-2}}$. Kauffmann & Pillai (2010) propose an empirical threshold $M(r) \geqslant 870\ M_\odot(r/\mathrm{pc})^{1.33}$ (dashed red line) as a minimum condition for massive star formation.

Columns (9) and (10) in Tables 2 and 3 mark whether robust or candidate MYSOs are greater than thresholds of $M(r) = 870\ M_\odot(r/\mathrm{pc})^{1.33}$ (hereafter threshold one) and $\Sigma_{crit} = 1\ \mathrm{g\ cm^{-2}}$ (hereafter threshold two). Robust and candidate MYSOs almost all both exceed threshold one but show significant differences under the threshold two criteria. About 36.7% of candidate MYSOs do not meet threshold two, but this proportion is only 22.5% of robust MYSOs. However, this ratio was significantly increased among non-MYSO candidates, and nearly 60% of them did not exceed threshold two. We infer that the reason for this difference in the ratios is that higher-density gas may provide higher accretion just like robust MYSOs, and lower gas mass and density are also difficult to provide a larger accretion rate, thus forming MYSOs. Column (11) in Tables 2 and 3 marks whether sources are associated with Class II methanol maser, which is one of the most reliable and sensitive tracers in the early stage of high-mass star formation region (Ellingsen 2006). Nearly 50% of robust MYSOs are associated with Class II methanol maser, and that about 27% of candidate MYSOs, which shows that the former as the MYSOs are more reliable than the latter.

5. Conclusions

We screened out the WISE objects with green features in the whole Galactic plane ($0° < l < 360°$ and $-2° < b < 2°$) and selected MYSOs sample with the help of SED fitting from mid-infrared to far-infrared and gravity thresholds. Our findings can be summarized as follows:

1. After crossmatching with the SIMBAD database to ensure non-YSO exclusions, we identified 2135 WGOs and divided them into three groups. The first group comprises 264 WGOs with an extended green structure, similar to the traditional Spitzer EGOs. 1366 WGOs without extended structures but showing compact green features are in the second group. The third group of 505 WGOs is neither extended nor visually green, but numerically W2(green)/W1(blue) is greater than 4.5.
2. We find that ∼75% WGOs are distributed in $|l| < 60°$, and in $|l| > 60°$ the distribution of the WGOs is consistent with known star-forming regions. The distribution of WGOs is positively correlated with the density of molecular gas, except in the ultradense gas region of the Galactic center. The WGOs have a Gaussian distribution along the Galactic latitude ($|b| < 2°$) but shift to negative Galactic latitude by $\sim 0.^\circ 1$.
3. 1260 WGOs have Hi-GAL source counterparts, accounting for 71% of the total in the Hi-GAL survey range. Spitzer/IRAS survey catalog shows a high association rate similar to that Hi-GAL catalog, over 54% WGOs matched successfully. However, the WISE and 2MASS, RMS, and ATLASGAL survey catalogs for YSOs show very low association rates with WGOs, 3.2%, 11.1%, and 20.8% respectively. By crossmatching with these three catalogs, we obtained 2067, 1635, and 1176 YSOs newly identified and 348 new MYSOs from the RMS MYSO subcatalog.
4. The WGOs in Group 1 are in the later evolutionary stage compared to the other two groups, as they have extended structures that are characteristic of outflow and a significantly higher rate of association with various

masers, in addition, physical parameters such as the luminosity of the parent structure and the gas accretion rate are significantly higher.

5. From SED fitting, we obtained the stellar mass $M_\star$ and accretion rate $\dot{M}_{\rm acc}$ of 1151 WGOs. The luminosity of WGOs in Group 1 is significantly larger than the other two. 231 WGOs with stellar mass $M_\star + \dot{M}_{\rm acc} \times 10^4\,{\rm yr} > 8\,M_\odot$ are selected as robust MYSOs. 172 WGOs with accretion rate $\dot{M}_{\rm acc} > 10^{-4}\,M_\odot\,{\rm yr}^{-1}$ are selected as candidate MYSOs. We find that the accretion rate and the density of the parent structure of WGOs are positively correlated.

We would like to thank the anonymous referees for the valuable comments, which improved the quality of the paper. We would to thank Dr. Zhiwei CHEN from Purple Mountain Observatory, Chinese Academy of Sciences for useful discussions on this paper. This work is supported by the Key Project of International Cooperation of Ministry of Science and Technology of China through grant 2010DFA02710, and by the National Natural Science Foundation of China through grants 11503035, 11573036, 11373009, 11433008, 11403040, and 11403041. G.Z. acknowledges support from the Postdoctoral Science Foundation of China (No. 2021T140672), and the National Natural Science Foundation of China (No. U2031118).

ORCID iDs

Chang Zhang https://orcid.org/0000-0001-7927-8539
Guo-Yin Zhang https://orcid.org/0000-0002-7254-669X

References

An, D., Ramírez, S. V., Sellgren, K., et al. 2011, ApJ, 736, 133
Andre, P., Ward-Thompson, D., & Barsony, M. 1993, ApJ, 406, 122
Arce, H. G., Shepherd, D., Gueth, F., et al. 2007, in Protostars and Planets V, ed. B. Reipurth, D. Jewitt, & K. Keil (Tucson, AZ: Univ. Arizona Press), 245
Bachiller, R. 1996, ARA&A, 34, 111
Barnes, A. T., Longmore, S. N., Battersby, C., et al. 2017, in IAU Symp. 322, The Multi-Messenger Astrophysics of the Galactic Centre, ed. R. M. Crocker, S. N. Longmore, & G. V. Bicknell (Cambridge: Cambridge Univ. Press), 147
Benjamin, R., Churchwell, E., Babler, B., et al. 2003, PASP, 115, 953
Bergin, E. A., & Tafalla, M. 2007, ARA&A, 45, 339
Beuther, H., Churchwell, E. B., McKee, C. F., & Tan, J. C. 2007, in Protostars and Planets V, ed. B. Reipurth, D. Jewitt, & K. Keil (Tucson, AZ: Univ. Arizona Press), 165
Bonnell, I., & Greaves, J. 2004, Spitzer Proposal, 3394
Bonnell, I. A., Bate, M. R., Clarke, C. J., & Pringle, J. E. 1997, MNRAS, 285, 201
Breen, S. L., Ellingsen, S. P., Contreras, Y., et al. 2013, MNRAS, 435, 524
Bressert, E., Ginsburg, A., Bally, J., et al. 2012, ApJL, 758, L28
Busso, M., Gallino, R., & Wasserburg, G. J. 1999, ARA&A, 37, 239
Butler, M. J., & Tan, J. C. 2012, ApJ, 754, 5
Caratti o Garatti, A., Stecklum, B., & Garcia Lopez, R. 2017, NatPh, 13, 276
Chen, X., Ellingsen, S. P., Shen, Z.-Q., Titmarsh, A., & Gan, C.-G. 2011, ApJS, 196, 9
Chen, X., Gan, C.-G., Ellingsen, S. P., et al. 2013, ApJS, 206, 9
Chen, Z., Sun, W., Chini, R., et al. 2021, ApJ, 922, 90
Cho, S.-H., Yun, Y., Kim, J., et al. 2016, ApJ, 826, 157
Churchwell, E., & GLIMPSE Team 2001, BAAS, 33, 821
Churchwell, E., Babler, B. L., Meade, M. R., et al. 2009, PASP, 121, 213
Cragg, D. M., Johns, K. P., Godfrey, P. D., & Brown, R. D. 1992, MNRAS, 259, 203
Crocker, R. M., Jones, D. I., Aharonian, F., et al. 2011, MNRAS, 413, 763
Csengeri, T., Weiss, A., Wyrowski, F., et al. 2016, A&A, 585, A104
Cyganowski, C. J., Brogan, C. L., Hunter, T. R., et al. 2017, MNRAS, 468, 3694
Cyganowski, C. J., Brogan, C. L., Hunter, T. R., & Churchwell, E. 2009, ApJ, 702, 1615
Cyganowski, C. J., Koda, J., Rosolowsky, E., et al. 2013, ApJ, 764, 61
Cyganowski, C. J., Whitney, B. A., Holden, E., et al. 2008, AJ, 136, 2391
Davis, C. J., Kumar, M. S. N., Sandell, G., et al. 2007, MNRAS, 374, 29
Elia, D., Merello, M., Molinari, S., et al. 2021, MNRAS, 504, 2742
Ellingsen, S. P. 2006, ApJ, 638, 241
Fazio, G. G., Hora, J. L., Allen, L. E., et al. 2004, ApJS, 154, 10
Furuya, R. S., Kitamura, Y., Wootten, A., Claussen, M. J., & Kawabe, R. 2003, ApJS, 144, 71
Gallimore, J. F., Cool, R. J., Thornley, M. D., & McMullin, J. 2003, ApJ, 586, 306
Greene, T. P., Wilking, B. A., Andre, P., Young, E. T., & Lada, C. J. 1994, ApJ, 434, 614
Hasegawa, T., Morita, K., Okumura, S., et al. 1986, in Masers, Molecules, and Mass Outflows in Star Formation Regions, ed. A. D. Haschick (Westford, MA: Haystack Observatory), 275
Heiderman, A., Evans, Neal, J., et al. 2010, ApJ, 723, 1019
Herbig, G. H. 1962, AdA&A, 1, 47
Herwig, F. 2005, ARA&A, 43, 435
Higuchi, A. E., Hasegawa, T., Saigo, K., Sanhueza, P., & Chibueze, J. O. 2015, ApJ, 815, 106
Hinz, J. L., Rieke, G. H., Yusef-Zadeh, F., et al. 2009, ApJS, 181, 227
Hoare, M. G., Lumsden, S. L., Oudmaijer, R. D., et al. 2005, in IAU Symp. 227, Massive Star Birth: A Crossroads of Astrophysics, ed. R. Cesaroni et al. (Cambridge: Cambridge Univ. Press), 370
Hollenbach, D., Elitzur, M., & McKee, C. F. 2013, ApJ, 773, 70
Hosokawa, T., Yorke, H. W., & Omukai, K. 2010, ApJ, 721, 478
Hunter, T. R., Brogan, C. L., De Buizer, J. M., et al. 2021, ApJL, 912, L17
Immer, K., Schuller, F., Omont, A., & Menten, K. M. 2012, A&A, 537, A121
Jijina, J., & Adams, F. C. 1996, ApJ, 462, 874
Jones, B. M., Fuller, G. A., Breen, S. L., et al. 2020, MNRAS, 493, 2015
Jones, O. C., Sharp, M. J., Reiter, M., et al. 2019, MNRAS, 490, 832
Kauffmann, J., & Pillai, T. 2010, ApJL, 723, L7
Kennicutt, R. C., & Evans, N. J. 2012, ARA&A, 50, 531
Kruijssen, J. M. D. 2012, MNRAS, 426, 3008
Krumholz, M. R., & McKee, C. F. 2008, Natur, 451, 1082
Kuhn, M. A., de Souza, R. S., Krone-Martins, A., et al. 2021, ApJS, 254, 33
Lada, C. J. 1987, in IAU Symp. 115, Star Forming Regions ed. M. Peimbert & J. Jugaku (Dordrecht: Springer), 1
Lada, C. J., & Lada, E. A. 2003, ARA&A, 41, 57
Lada, C. J., Lombardi, M., & Alves, J. F. 2010, ApJ, 724, 687
Ladeyschikov, D. A., Bayandina, O. S., & Sobolev, A. M. 2019, AJ, 158, 233
Larson, R. B. 1981, MNRAS, 194, 809
López-Sepulcre, A., Cesaroni, R., & Walmsley, C. M. 2010, A&A, 517, A66
Lumsden, S. L., Hoare, M. G., Urquhart, J. S., et al. 2013, ApJS, 208, 11
Mac Low, M.-M., Elitzur, M., Stone, J. M., & Konigl, A. 1994, ApJ, 427, 914
Marton, G., Tóth, L. V., Paladini, R., et al. 2016, MNRAS, 458, 3479
Matsuura, M., Yamamura, I., Murakami, H., et al. 2000, PASJ, 52, 895
McKee, C. F., & Tan, J. C. 2002, Natur, 416, 59
McKee, C. F., & Tan, J. C. 2003, ApJ, 585, 850
Mège, P., Russeil, D., Zavagno, A., et al. 2021, A&A, 646, A74
Molinari, S., Brand, J., Cesaroni, R., & Palla, F. 1996, A&A, 308, 573
Molinari, S., Swinyard, B., Bally, J., et al. 2010, PASP, 122, 314
Moser, E., Liu, M., Tan, J. C., et al. 2020, ApJ, 897, 136
Motte, F., Bontemps, S., & Louvet, F. 2018, ARA&A, 56, 41
Nakashima, J.-i., & Deguchi, S. 2000, PASJ, 52, L43
Noriega-Crespo, A., Morris, P., Marleau, F. R., et al. 2004, ApJS, 154, 352
Olivier, G. M., Lopez, L. A., Rosen, A. L., et al. 2021, ApJ, 908, 68
Pilbratt, G. L., Riedinger, J. R., Passvogel, T., et al. 2010, A&A, 518, L1
Reach, W. T., Rho, J., Tappe, A., et al. 2006, AJ, 131, 1479
Reid, M. J. 2002, in IAU Symp. 206, Cosmic Masers: From Proto-Stars to Black Holes, ed. V. Migenes & M. J. Reid (San Francisco, CA: ASP), 506
Robitaille, T. P. 2017, A&A, 600, A11
Robitaille, T. P., Whitney, B. A., Indebetouw, R., Wood, K., & Denzmore, P. 2006, ApJS, 167, 256
Sanhueza, P., Jackson, J. M., Foster, J. B., et al. 2012, ApJ, 756, 60
Schmidt, M. 1959, ApJ, 129, 243
Schuller, F., Menten, K. M., Contreras, Y., et al. 2009, A&A, 504, 415
Shu, F. H., Adams, F. C., & Lizano, S. 1987, ARA&A, 25, 23
Smith, M. D., & Rosen, A. 2005, MNRAS, 357, 1370
Smith, R. J., Longmore, S., & Bonnell, I. 2009, MNRAS, 400, 1775
Snyder, L. E., & Buhl, D. 1974, ApJL, 189, L31

Sobolev, A. M., Cragg, D. M., Ellingsen, S. P., et al. 2007, in IAU Symp. 242, Astrophysical Masers and their Environments (Cambridge: Cambridge Univ. Press), 81
Stecklum, B., Heese, S., Wolf, S., et al. 2017, arXiv:1712.01451
Stecklum, B., Wolf, V., Linz, H., et al. 2021, A&A, 646, A161
Szymczak, M., Pillai, T., & Menten, K. M. 2005, A&A, 434, 613
Tout, C. A., Pols, O. R., Eggleton, P. P., & Han, Z. 1996, MNRAS, 281, 257
Towner, A. P. M., Brogan, C. L., Hunter, T. R., et al. 2017, ApJS, 230, 22
Towner, A. P. M., Brogan, C. L., Hunter, T. R., Cyganowski, C. J., & Friesen, R. K. 2019, ApJ, 875, 135
Urquhart, J. S., Moore, T. J. T., Csengeri, T., et al. 2014, MNRAS, 443, 1555
Urquhart, J. S., Wells, M. R. A., Pillai, T., et al. 2022, MNRAS, 510, 3389
Velusamy, T., Langer, W. D., & Marsh, K. 2007, ApJL, 668, L159
Wang, Y., Beuther, H., Bik, A., et al. 2011, A&A, 527, A32
Wenger, M., Ochsenbein, F., Egret, D., et al. 2000, A&AS, 143, 9
Wright, E. L., Eisenhardt, P. R. M., Mainzer, A. K., et al. 2010, AJ, 140, 1868
Wright, E. L., Eisenhardt, P. R. M., Mainzer, A. K., et al. 2019, AllWISE Source Catalog, IPAC doi:10.26131/IRSA1
Yorke, H. W., & Sonnhalter, C. 2002, ApJ, 569, 846
Yusef-Zadeh, F., Hewitt, J. W., Arendt, R. G., et al. 2009, ApJ, 702, 178
Zapata, L. A., Menten, K., Reid, M., & Beuther, H. 2009, ApJ, 691, 332
Zhang, C., Zhang, G.-Y., Li, J.-Z., & Li, X.-M. 2022, RAA, 22, 055012
Zhang, G.-Y., Xu, J.-L., Vasyunin, A. I., et al. 2018, A&A, 620, A163
Zhang, Y., & Tan, J. C. 2011, ApJ, 733, 55
Zinnecker, H., & Yorke, H. W. 2007, ARA&A, 45, 481